RESEARCH ARTICLE

Society For Biomaterials · WILEY

Ibuprofen-loaded bilayer electrospun mesh modulates host response toward promoting full-thickness abdominal wall defect repair

Jiajie Liu[1] | Rui Tang[1] | Xiaoqiang Zhu[1] | Qiaolin Ma[2] | Xiumei Mo[2] | Jinglei Wu[2] | Zhengni Liu[1,3]

[1]Department of Hernia and Abdominal Wall Surgery, Shanghai East Hospital, Tongji University, Shanghai, People's Republic of China

[2]Shanghai Engineering Research Center of Nano-Biomaterials and Regenerative Medicine, College of Biological Science and Medical Engineering, Donghua University, Shanghai, People's Republic of China

[3]Department of General Surgery, Shanghai East Hospital Ji'an Hospital, Ji'an, Jiangxi Province, People's Republic of China

Correspondence
Jinglei Wu, Shanghai Engineering Research Center of Nano-Biomaterials and Regenerative Medicine, College of Biological Science and Medical Engineering, Donghua University, Shanghai 201620, People's Republic of China.
Email: jw@dhu.edu.cn

Zhengni Liu, Department of Hernia and Abdominal Wall Surgery, Shanghai East Hospital, Tongji University, 150 Ji Mo Road, Shanghai 200120, People's Republic of China.
Email: liuzhengni@tongji.edu.cn

Abstract

Pro-inflammatory response impairs the constructive repair of abdominal wall defects after mesh implantation. Electrospinning-aid functionalization has the potential to improve the highly orchestrated response by attenuating the over-activation of foreign body reactions. Herein, we combined poly(L-lactic acid-co-caprolactone) (PLLA-CL) with gelatin proportionally via electrospinning, with Ibuprofen (IBU) incorporation to fabricate a bilayer mesh for the repair improvement. The PLLA-CL/gelatin/IBU (PGI) mesh was characterized in vitro and implanted into the rat model with a full-thickness defect for a comprehensive evaluation in comparison to the PLLA-CL/gelatin (PG) and off-the-shelf small intestinal submucosa (SIS) meshes. The bilayer PGI mesh presented a sustained release of IBU over 21 days with degradation in vitro and developed less-intensive intraperitoneal adhesion along with a histologically weaker inflammatory response than the PG mesh after 28 days. It elicited an M2 macrophage-dominant foreign body reaction within the process, leading to a pro-remodeling response similar to the biological SIS mesh, which was superior to the PG mesh. The PGI mesh provided preponderant mechanical supports over the SIS mesh and the native abdominal wall with similar compliance. Collectively, the newly developed mesh advances the intraperitoneal applicability of electrospun meshes by guiding a pro-remodeling response and offers a feasible functionalization approach upon immunomodulation.

KEYWORDS
abdominal wall defect repair, bilayer mesh, electrospinning, host response, ibuprofen, immunomodulation

1 | INTRODUCTION

To date, there are more than 20 million hernia repair procedures per year worldwide.[1] Surgical meshes have been applied in most operations, which have evidently become the standard of care for all kinds of abdominal wall defects.[2] Over the past six decades, mesh products

have evolved from synthetic materials and nature matrices toward engineered composites derived from diverse sources, aiming to retrieve the integrity of the abdominal wall morphemically and functionally.[3] However, the "double-edged sword" issue of a successful repair by using meshes has yet to be well addressed. The mechanically robust mesh commonly triggers a chronic foreign body reaction (FBR) followed by ineffective integration, resulting in progressively fibrotic healing.[4] Alternatively, the biological mesh facilitates host integration

Jiajie Liu and Rui Tang contributed equally to this work.

in terms of solid extracellular matrix (ECM) remodeling, whereas they mostly yield rupture at the tissue-mesh interface followed by bulging at the center of mesh, leading to a fatal repair failure.[5]

Host response to the surgical mesh is a critical determinant of repair success or failure. This highly orchestrated process is broadly classified into acute inflammation, chronic inflammation, FBR, and fibrosis or reconstruction.[6] FBR, associated with a localized sustaining inflammation elicited by the meshes, commonly develops stiff healing that may confer certain complications, including postoperative pain and discomfort, dysfunction restoration, and even mesh explantation.[7,8] In contrast, the pro-remodeling response typically facilitates a constructive repair after the inflammatory phase.[9] At the cellular level, the response is composed of a transient neutrophil accumulation followed by an intensive accumulation of macrophages within and around the mesh, in which different macrophage phenotypes play critical and diverse roles in the process.[10] The underlying mechanisms revealed that T-helper 1 (Th-1) cell activation induces a pro-inflammatory activation through the activated M1 macrophage phenotype during the inflammatory phase. Sequentially, macrophages fuse into foreign body giant cells (FBGCs) as a hallmark of FBR and remain in the meshes to form a fibrotic encapsulation eventually. Whereas the macrophages could be polarized to the activated M2 phenotype driven by T-helper 2 (Th-2) cell activation to participate in a positive pro-remodeling event by secreting various growth factors and cytokines.[11] This state-of-affair favors switching macrophage polarization from the M1 to M2 phenotype as a promising strategy to achieve a constructive repair. For instance, different types of ECM proteins and stem cells have been coated onto the polypropylene mesh to alleviate FBR. However, their immunomodulatory roles in the process remain controversial, and they seemingly have fallen far short of surgical safety, cost, and handling.[12,13]

Regarding the clinical feasibility, increasing attention has been paid to optimizing the mesh with anti-inflammatory properties for improved responses. The functionalization is commonly achieved by conferring antibiotics, antiseptics, or therapeutic genes to the mesh in a bid to reduce mesh-related inflammation.[14,15] Ibuprofen (IBU) is a nonsteroid antiphlogistic drug, an effective anti-cyclooxygenase-1 compound, with anti-inflammatory, anti-adhesive, and pain relief properties.[16] More importantly, IBU stimulates T cell recruitment and macrophage polarization by reducing pro-inflammatory cytokine expression and enhancing Th1-associated cytokine expression.[17] These features propose the fabrication of an IBU-loaded scaffold as a controlled release system to inhibit excessive inflammation and adhesion in the context of tissue repair. Electrospinning has gained attention for its simple processability and versatility in fabricating ECM-mimicking scaffolds. Biodegradable structures tailored with a high surface area capable of IBU loading and release have been reported in muscle wound healing, nerve regeneration, and anti-adhesion barriers.[18-20] However, a similar application has yet been well documented in abdominal wall defect repair, especially the nanofibrous layer favoring visceral anti-adhesion is commonly doubtful to promote tissue integration in a single-layer mesh. Hence, it is of paramount interest to fabricate a bilayer mesh, in which the administration

of IBU from a nanofiber layer tailored with a smooth and biocompatible surface prevents intraperitoneal adhesion under limited inflammatory response, and the micron-sized porous structure promotes abdominal wall remodeling by modulating macrophage polarization concurrently. In this scenario, the preparation with U.S. Food and Drug Administration (FDA)-approved materials are preferable. More importantly, the performance of this electrospun mesh should be tantamount to that of a clinically paradigmatic biomaterial, which is superior to typical polymeric meshes upon the host response under intraperitoneal repair.[21] Of note, several studies have shown that the small intestinal submucosa (SIS) mesh is infiltrated with a greater proportion of M2 macrophage than the synthetic meshes. It is considered that the recruitment of endogenous stem cells, growth factor sequestration, and release of bioactive fragments with degradation all contribute to modulating macrophage polarization in the innate immune response.[22] Therefore, the clinically commercial SIS mesh (Biodesign®), consisting of compressed 4-layer SIS, is an appropriate control for evaluating the host response compared to the newly developed mesh in this study.

Building on our previous work, poly(L-lactic acid-co-caprolactone) (PLLA-CL) could be combined with gelatin to optimize the electrospun template owing to their physicochemical and mechanical superiorities in tissue repair.[23] To this end, we fabricated a functional electrospun mesh by combining PLLA-CL with gelatin to load IBU proportionally in this study. The bilayer structure is expected to provide an IBU-loading nanofibrous layer facing peritoneal cavity that alleviates intraperitoneal inflammation and adhesion, and a nanofibers-twisted yarn layer facing the abdominal wall that facilitates cell infiltration and tissue remodeling. The PLLA-CL/gelatin/IBU (PGI) mesh was comprehensively evaluated by repairing the full-thickness defects of rats for 28 days. The analysis of intraperitoneal adhesion formation with the spatiotemporal host response to the meshes and mechanical performance are detailed and discussed by comparing with the performances of PLLA-CL/gelatin (PG) mesh and clinically commercial SIS mesh. We hypothesized that the innovative mesh could yield an effective pro-remodeling response by reducing FBR, leading to mechanically sufficient repair, and providing a potentially applicable solution for the constructive repair of the abdominal wall defects.

2 | MATERIALS AND METHODS

2.1 | Materials

Type A gelatin (gel strength ~300 g Bloom) was obtained from Sigma–Aldrich. PLLA-CL (LA: CL = 75:25) was obtained from Daigang Biomaterial Co., Ltd. (Jinan, China). Decellularized porcine SIS mesh, as a clinically available biological mesh (Biodesign®), was obtained from Cook Medical (Bloomington, In, USA). IBU was obtained from Shanghai Macklin Biochemical Co., Ltd (Shanghai, China). Mouse monoclonal anti-CD31, anti-CD86, rabbit polyclonal anti-collagen I, rabbit monoclonal anti-CD11b, anti-alpha smooth muscle actin (α-SMA) antibodies, and glyceraldehyde 3-phosphate dehydrogenase

(GAPDH) were purchased from Abcam, Inc. (Cambridge, MA, USA). Mouse monoclonal anti-CD206 and anti-elastin antibodies were obtained from Santa Cruz, Inc. (Dallas, TX, USA). Mouse monoclonal anti-CD68 antibodies were obtained from Arigo, Inc. (Taiwan, China). Recombination human tumor necrosis factor α (TNF-α) and interleukin 6 (IL-6) multiplex ELISA kits were obtained from MultiSciences Biotech Co., Ltd. (Hangzhou, China).

2.2 | Preparation and characterization of electrospun meshes

Bilayer meshes were prepared via a two-step electrospinning according to our previous reports with modifications.[23] Briefly, PLLA-CL and gelatin were separately dissolved in 1,1,1,3,3,3-hexafluoro-2-propanol (HFIP) (Da-Rui Co. Ltd., China) and mixed to yield a 12% (w/v) solution with PG ratio of 8:2 for electrospinning. A volume of 10 mL PG solution was fed at 1.2 mL h^{-1} and charged with a 12 kV voltage to generate nanofibers, which were twisted into yarns through a water vortex and finally collected by a rotating mandrel (10 cm diameter, 60 rpm) to obtain nanofiber yarn membrane as previously described.[24] The obtained nanofiber yarn layer was lyophilized and wrapped on the surface of a slow-rotating mandrel (10 cm diameter, 120 rpm) to collect random nanofibers. For the preparation of a random nanofiber layer, 6 mL PG solution was blended with 0.2% (w/v) IBU to generate random nanofibers. PGI nanofibers were deposited on the surface of the nanofiber yarn layer to prepare a bilayer mesh. A bilayer mesh composed of a nanofiber yarn layer and a PG nanofiber layer without IBU (PG) was prepared and served as a control.

The bilayer morphology with cross-section structure was observed by scanning electron microscopy (SEM; Hitachi, TM-1000, Japan). Fiber diameters and distributions were measured by calculating one hundred single fibers from two independent images using ImageJ software (NIH, Bethesda, MD, USA). The mesh thickness was calculated based on the SEM images by measuring the thickness of 10 random cross-sections. The water contact angles of the meshes from different layers were analyzed with a contact angle instrument (OCA40, DataPhysics, Germany).

Bilayer meshes were tailored into rectangular strips (4 × 1 cm) and mounted in the grips of a uniaxial testing machine (Instron 5567, Norwood, MA) with a 50 N load and stretched at a crosshead speed of 5 mm min^{-1} until failure. The corresponding stress–strain curves were recorded, and Young's modulus (MPa) was calculated from the linear slope of the stress–strain curve (n = 4). Elongation data represent that the sample tolerates an increased stretch before breakage, and the ultimate tensile strength was calculated as the maximal load divided by the cross-sectional area (MPa). Clinically available SIS mesh was also tested as a control.

To evaluate the degradation, 50 mg of each mesh was added to 10 mL of phosphate-buffered saline (PBS) containing 0.02% sodium azide and 0.1 μg mL^{-1} proteinase K (Sigma–Aldrich, USA) and incubated in a concussion incubator (5 rpm, 37°C) for 30 days. Samples were taken every 7 days and rinsed with deionized water to remove residual buffer salts followed by lyophilization. The mass loss was recorded to calculate the remaining mass compared to the original mass (%). Each sample was measured three times, and the average results were calculated. After 28 days of degradation in vitro, the mesh morphology was observed by SEM.

2.3 | IBU load and release

The amount of the IBU in the obtained PG solution was calculated by a UV–Vis spectrophotometer (Perkin Elmer, USA) at 264 nm; afterward, the loading efficiency of the IBU in the PGI nanofibers was calculated as follow: Loading efficiency $= \left(\frac{\text{mass of adsorbed IBU in the solution}}{\text{mass of total IBU}}\right) \times$ 100%. The release profile of IBU from the PGI bilayer mesh was determined by UV spectrophotometry. Briefly, the bilayer mesh was tailored into small pieces (approximately 50 mg per sample) and immersed in 2 mL of PBS (10 mM, pH = 7.4) and incubated at 37°C under static conditions (n = 4). At predetermined time intervals of up to 21 days, 1 mL PBS was collected for analysis and fresh aliquot of PBS was replenished for continuing incubation. The released IBU from the bilayer mesh was determined using a UV–Vis spectrophotometer at 264 nm. A linear correlation (R^2 = .99) was obtained using absorbance versus IBU concentration of standard samples (0, 0.5, 1, 2, 5, and 10 μg mL^{-1}).

2.4 | Cytocompatibility evaluation of electrospun meshes

NIH 3T3 fibroblasts were used for in vitro evaluation, which were kindly provided by the Cell Bank of Chinese Academy of Science. Electrospun meshes were punched into discs with 6-mm diameter and placed in a 24-well plate. Disc samples were immersed in 70% ethanol for 1 h and then irradiated under UV (12 h for each side) for disinfection. NIH 3T3 fibroblasts were seeded onto the nanofiber and yarn surface of PG and PGI meshes, respectively, at a density of 1×10^5 cells per well. Cell culture was maintained in a 37°C incubator with 95% humidity and 5% CO_2. The medium was refreshed every other day.

After 1 and 4 days, the cell viability was evaluated by live/dead staining and CCK-8 assay. Cell-seeded PG and PGI were stained with calcein-AM and propidium iodide for 30 min at 37°C and visualized by a fluorescence microscope (DMi 8, Leica, Germany). For proliferative assessment, cell-seeded meshes were incubated with CCK-8 assay at 37°C for 1.5 h, and then 100 μL supernatant of each well was read at 450 nm using a plate reader (Multiskan MK3, Thermo, USA) (n = 9). The morphology of NIH 3T3 fibroblasts on different sides of electrospun meshes was observed by SEM. Samples were rinsed with PBS, fixed with 4% paraformaldehyde, dehydrated with gradient ethanol, and dried at room temperature. After sputter-coating with gold, samples were observed under a SEM (Phenom, Netherlands).

2.5 | Implantation and postoperative care

Mesh implantation was performed in accordance with the National Institutes of Health's Guide for the Care and Use of Laboratory Animals (NIH Publication N01-OD-4-2139, Rev. 2). Eighteen 8-week-old male Sprague–Dawley rats, weighing 200-250 g, were obtained from SLAC National Rodent Laboratory Animal Resources (Shanghai, China). The Institutional Review Committee of Shanghai Tongji University School of Medicine approved all animal study protocols (SYXK2020-0002). Under anesthesia induced by an intraperitoneal injection of 1% pentobarbital solution (0.1 mg g^{-1}), the rats were shaved and disinfected with povidone-iodine solution around the surgical fields. A skin incision (30 mm in length) was made along the linea alba, following a full-thickness defect at a size of 20×10 mm^2 was created. Afterwards, SIS, PG, or PGI mesh at a size of 30×20 mm^2, was randomly implanted into each rat ($n = 6$). For the electrospun mesh, the side of nanofiber layer with or without IBU was implanted to face the intraperitoneal cavity. The meshes were intermittently sutured to the abdominal fascia with a 3–0 polypropylene suture (Ethicon, USA) by overlapping the edge of the defect at 5 mm, following skin closures using 5–0 Vicryl interrupted sutures (Ethicon, USA). No antibiotic prophylaxis and analgesic treatment were administered after surgery. The performance of rats after native defect being created without mesh repair was also recorded ($n = 6$).

2.6 | Macroscopic observation

Three rats of each group were harvested randomly at 7 and 28 days after implantation with an intravenous injection of thiopental for the evaluation of host response and remodeling. Signs of infection, bulge, or herniation at the repairing site were recorded during the experiments. Seven days after the implantation, fluid samples from intraperitoneal exudation were reserved and centrifuged to measure the levels of inflammatory cytokines with ELISA kits, including TNF-α and IL-6. Visceral adhesion upon tenacity was scored by two investigators blinded to group assignment, according to the table as described by Jenkins et al. (Table S1).[25] The surface area of visceral adhesion was further calculated in percentage (%) by normalizing it to the original mesh area. The mesh dimensions were measured to assess possible intracorporeal shrinkage or expansion, and the proportional change in thickness was calculated by measuring the thickness of 10 random sites over the central area of the mesh. The meshes were retrieved together with the surrounding muscular abdominal wall as the explants and then prepared by paraffin embedding for further examination.

2.7 | Histological analysis

For histological analysis, hematoxylin and eosin (H&E) staining was performed to observe the host cell recruitment and infiltration, and the organization and deposition of collagen were evaluated by Masson's trichrome staining after 7 and 28 days. The inflammations

represented by leukocyte infiltration were analyzed by anti-CD11b (1:200) staining after 7 and 28 days. Anti-CD68 (1:200) staining was performed to evaluate the host immune response characterized by macrophage recruitments and infiltrations after 28 days. Within the same periods, anti-CD86 (1:300) and anti-CD206 (1:100) staining were used to assess the M1 and M2 subtypes of macrophage, respectively. The vascularization of the explants was observed by anti-CD31 (1:200) immunofluorescent staining after 28 days. Collagen I (1:100), elastin (1:100), and α-SMA (1:100) staining were visualized to reflect the ECM remodeling upon strengthened and elastic features. The numbers of positively stained cells or vessels were quantified and normalized to the tissue area (mm^2) by performing counts in 10 microscopy fields per sample. Similarly, the mean area of positive staining was normalized to the tissue area (%). Data were analyzed by two blinded investigators with ImageJ software (NIH, Bethesda, MD). To further quantify the specific indictors related to the development of FBR and remodeling, the proteins were extracted from the homogenates and western blotting was performed to determine their expression levels. The proteins were probed with antibodies directed against CD11b (1:1000), CD68 (1:1000), CD86 (1:1000), CD206 (1:200), and GAPDH (1:1000; Sigma). The immunoblotted protein bands were observed using a Prime enhanced chemiluminescence kit (Sigma, St. Louis, MO).

2.8 | Mechanical properties measurements ex vivo

The mechanical properties of the explants were measured with a mechanical testing system as previously described. The explants were tailored into 30×10 mm^2 strips longitudinally ($n = 5$) and immersed in PBS for 2 h to maintain their wettability before testing. The length of the sample held between two grips was set at 20 mm and then stretched along their longitudinal axes at a speed of 10 mm min^{-1} until failure. The corresponding stress–strain curves were recorded, and the ultimate tensile strength, Young's modulus, and elongation at break were calculated.

2.9 | Statistical analysis

Data are expressed as the mean ± standard deviation (SD). Significant differences were assessed by one-way analysis of variance (ANOVA), followed by pairwise post hoc analysis with Bonferroni correction. The tests were repeated at least three times to obtain the SD. SPSS 22.0 software was used for all statistical analyses. The p value <.05 was considered to indicate statistically significant differences.

3 | RESULTS

3.1 | Characterization of bilayer meshes

After electrospinning nanofiber layer onto the cylindrical mold wrapped by PLLA-CL/gelatin yarn layer, the PG and PGI meshes were

WILEY
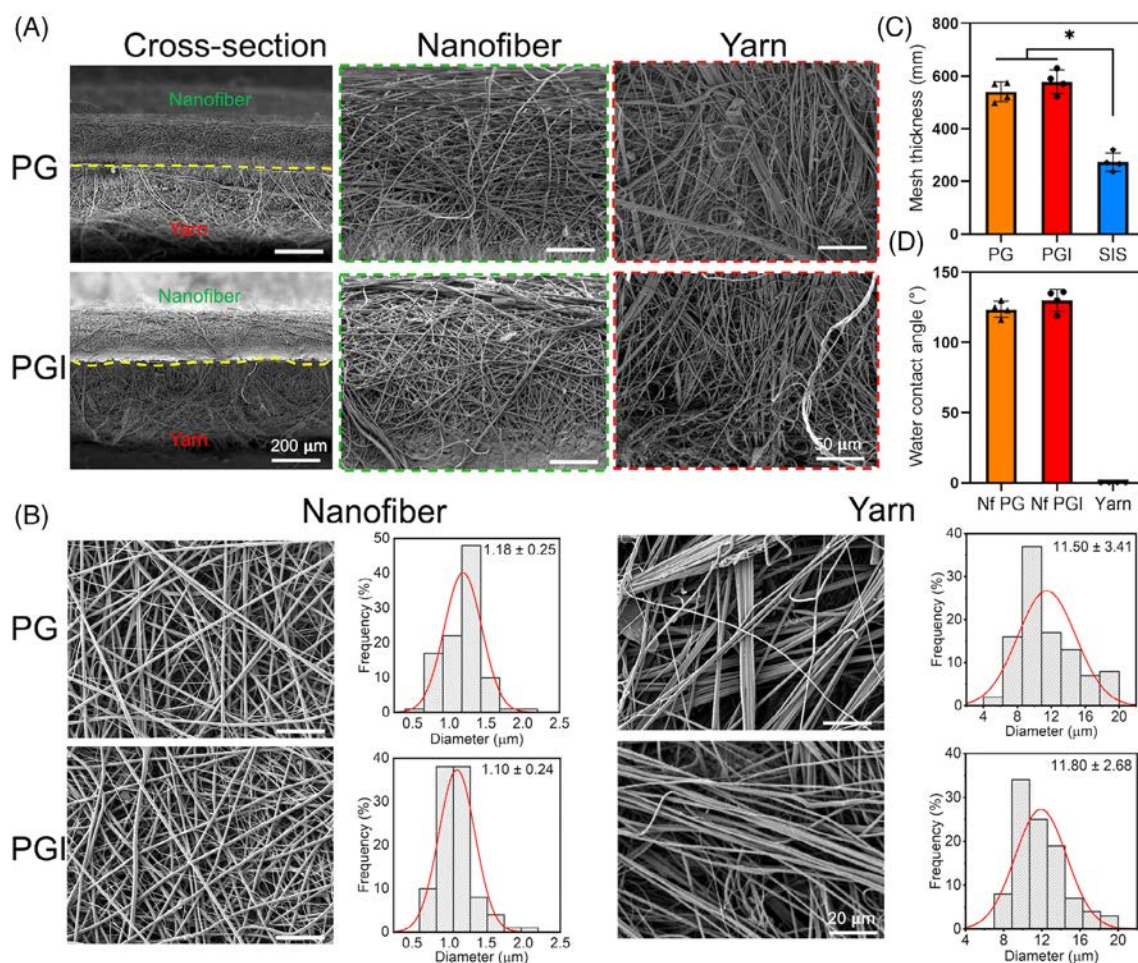
FIGURE 1 Structural characterization of bilayer meshes (A) representative scanning electron microscopy (SEM) images of PG and PGI meshes at cross-section; (B) representative SEM images of PG and PGI meshes from different sides and diameter distribution of nanofiber and yarn layers; (C) measurements of mesh thickness; and (D) measurements of water contact angle for meshes. Nf indicated nanofiber surface in (D). $n = 4$. *$p < .05$. IBU, Ibuprofen; PGI, PLLA-CL/gelatin/IBU; PLLA-CL, poly(L-lactic acid-co-caprolactone).

prepared. Cross-section images show that PG and PGI meshes presented similar bilayer structures, which were distinguished obviously along the boundary of different layers and maintained compact without obvious delamination (Figure 1A). Representative SEM images of nanofiber layers show that both PG and PGI meshes formed homogeneous and nanofibrous structures with fiber diameter being slightly affected after the addition of IBU (Figure 1B; $p > .05$). In contrast, the yarn layer of the meshes presented a harsher appearance composed of bundles of straight nanofibers with greater fiber diameters ($p < .05$). The measurements of mesh thickness indicate that both PG (542 ± 38 μm) and PGI (580 ± 48 μm) meshes showed similar values, which were thicker than the compressed SIS (272 ± 36 μm) mesh (Figure 1C; $p < .05$). The superficial and cross-sectioned morphologies of SIS were also observed (Figure S1). The hydrophobicity of the nanofiber layer was rarely affected by integrating IBU as the water contact angle increased from 123 ± 6° to 130 ± 7° with no significant difference ($p > .05$), while the values of yarn layer were 0° owing to the porous surface with large pore sizes (Figure 1D).

Mechanical properties of the meshes were evaluated comparatively. The PGI and PG meshes generated similar stress–strain curves,

while the SIS mesh generated a more compliant curve (Figure 2A). All the meshes provided comparable ultimate tensile strength (Figure 2B) and elongation of break (Figure 2C) with no significant difference ($p > .05$). Specifically, both PG and PGI meshes showed yield points of about 4 MPa and plateaus of approximately 6 MPa, of which the latter is due to the distinct layers of meshes. The ultimate tensile strength of the electrospun mesh is superior to the values of human transversalis fascia and posterior rectus sheath, indicating the strength supports sufficient for abdominal wall repair.[26] Young's moduli of PG and PGI meshes were higher than that of SIS ($p < .05$, Figure 2D). It indicated the collagen and elastic fibers that remain in SIS are more flexible than the uniformly straight fibers assembled in PG and PGI meshes.

After 4 weeks of incubation in vitro, the mesh remained generally structural integrity without obvious deformation. Locally, the nanofiber layer of the PGI mesh seems to develop more deformation than the counterpart of the PG mesh (Figure 2E). The residual weight of the PG and PGI meshes dropped to 91.0% ± 1.3% and 89.0% ± 0.9%, respectively, with no significant difference being found between them ($p > .05$, Figure 2F).
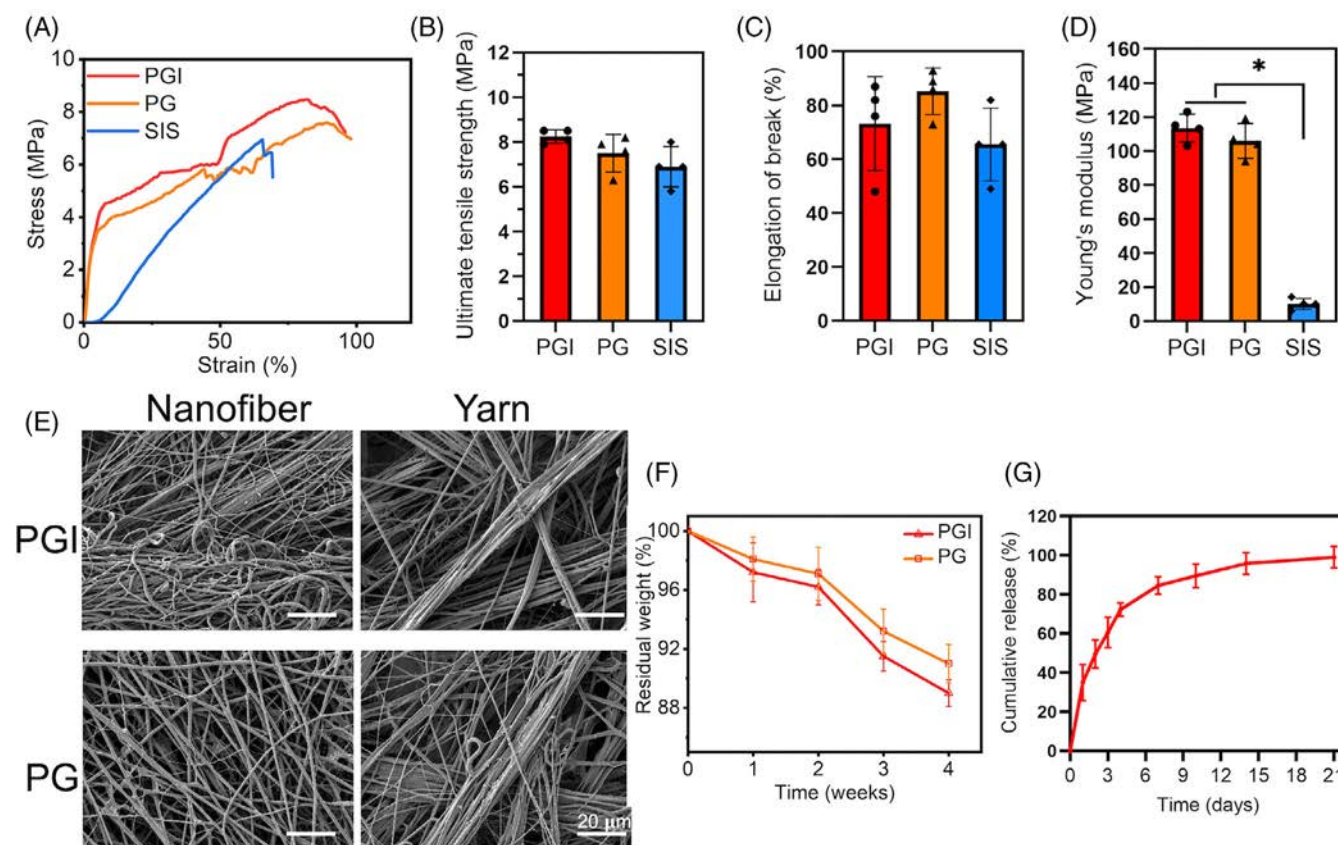
FIGURE 2 Mechanical measurements of bilayer meshes and SIS mesh and the degradation of electrospun structure with IBU release (A) representative stress–strain curves; (B) ultimate tensile strength; (C) elongation of break; (D) Young's modulus; (E) mesh morphology after 4-week degradation; (F) residual weight of mesh within 4-week degradation; and (G) IBU cumulative release profiles from PGI mesh within 21 days. $n = 4$. *$p < .05$. IBU, Ibuprofen; PGI, PLLA-CL/gelatin/IBU; PLLA-CL, poly(L-lactic acid-co-caprolactone); SIS, small intestinal submucosa.

3.2 | IBU load and release

According to the formula, the loading efficiency of IBU in the PG solution was on average 77.63%. An early burst release of IBU from the PGI bilayer mesh was observed (Figure 2G). More than 70% of IBU has been released after 4 days of incubation due to the diffusion of hydrophobic IBU from nanofibers and the lack of chemical interaction between IBU and PG nanofibers. Afterward, IBU from the mesh developed to a relatively slow-release period and reached proximity to complete release until 21 days.

3.3 | Cytocompatibility evaluation of electrospun meshes in vitro

The cytocompatibility of meshes was determined by cellular adhesion and proliferation, including live/dead staining, SEM, and CCK-8 assay. The images of live/dead staining indicated that fibroblasts were predominately alive (green) with a few dead cells (red) on both nanofiber and yarn surfaces of PG and PGI meshes on days 1 and 4 after culture (Figure 3A). SEM images showed that fibroblasts firmly attached to the electrospun surface on day 1 and formed local confluence with

clear cytoskeletons presented connectedly on the meshes on day 4. Cells on the yarn surface of meshes proliferated and spread in an oriented manner based on the structures (Figure 3B). The cell viability of nanofiber surface of PG meshes was similar to the value of PGI on day 1, while the steady trend of proliferation on PGI deteriorated slightly owing to the release of IBU after 4 days. There was no significant difference between the cell viability of the two groups during this period ($p > .05$; Figure 3C). Similar results of the comparison were also confirmed between the yarn layers of PG and PGI meshes without IBU involved ($p > .05$; Figure 3D).

3.4 | Macroscopic observation and inflammatory evaluation

As shown in Figure 4A, the meshes at a size of $30 \times 20 \text{ mm}^2$, including SIS, PG, and PGI, were implanted to repair the defect. In the follow-up, two rats implanted with the PG mesh presented evidence of incisional infection 7 days post-surgery. After 28 days, the rats implanted with PG and PGI meshes recovered from surgery and demonstrated no apparent signs of bulge or herniation on the abdominal wall side, while one SIS-repaired rat developed a large ventral hernia
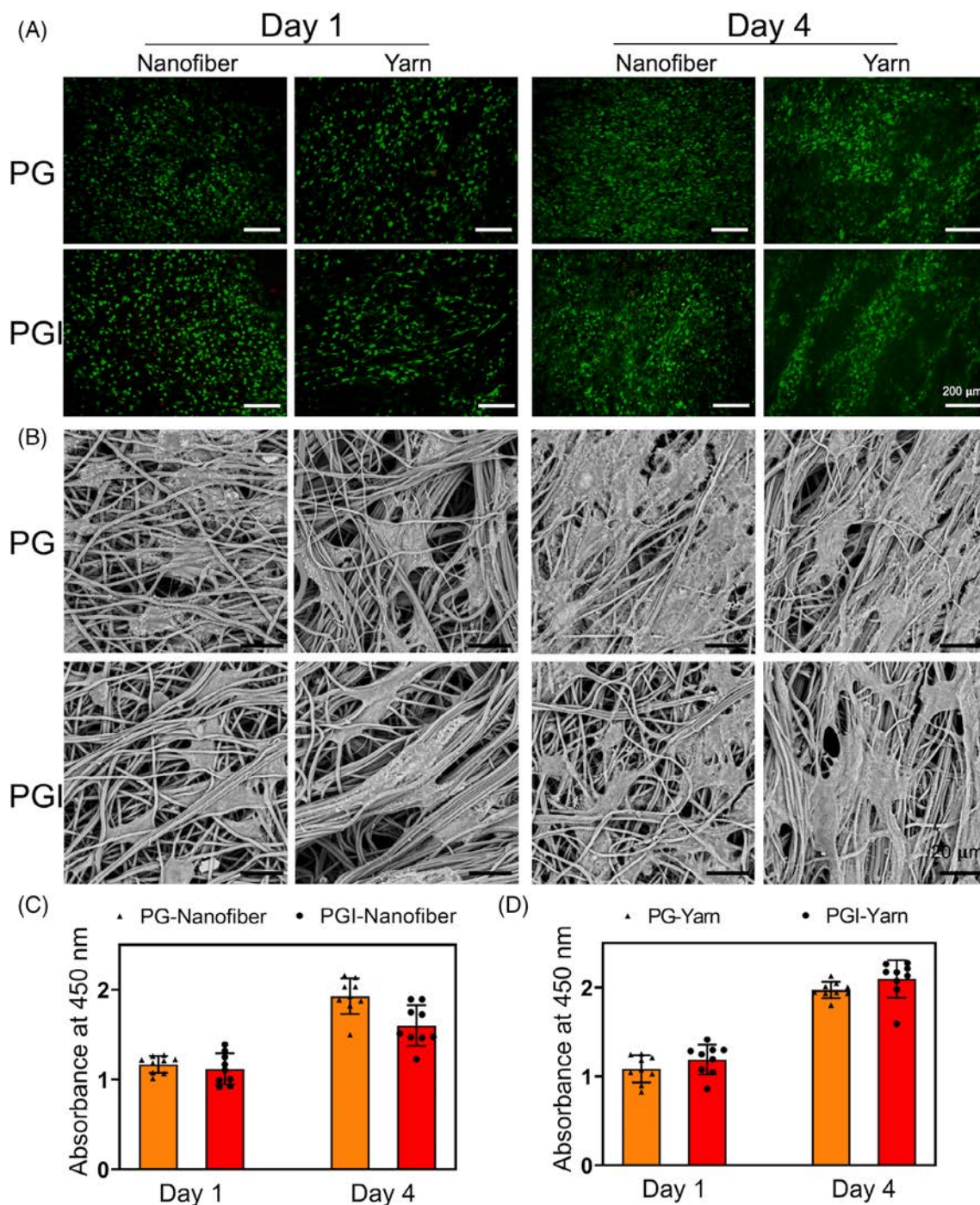
FIGURE 3 Cytocompatibility evaluation of electrospun meshes in vitro (A) representative Live/dead staining on day 1 and day 4; (B) observation of fibroblasts attachment on various surfaces of meshes by scanning electron microscopy; (C, D) the proliferation of fibroblasts seeded on nanofiber and yarn surface of meshes on day 1 and day 4. $n = 9$. *$p < .05$. IBU, Ibuprofen; PGI, PLLA-CL/gelatin/IBU; PLLA-CL, poly(L-lactic acid-co-caprolactone).

(Figure S2). All the defect-created rats without mesh covered expectedly developed ventral hernia after 28 days. Macroscopically, there were no aggressive responses observed on the abdominal side of the mesh-repaired rats. However, various extents of intraperitoneal adhesion were observed in the intraperitoneal side of SIS and PG explants with anchor points that needed sharp dissection.

All the meshes after implantation shrank by surface area, in which the SIS mesh showed a higher percentage of shrinkage than PG and PGI meshes after 28 days ($p < .05$; Figure 4B). All the retrieved explants became thicker than the original meshes and the defect created without mesh repair as a control, and the PG explants developed a greater increase in thickness compared with the other two groups of
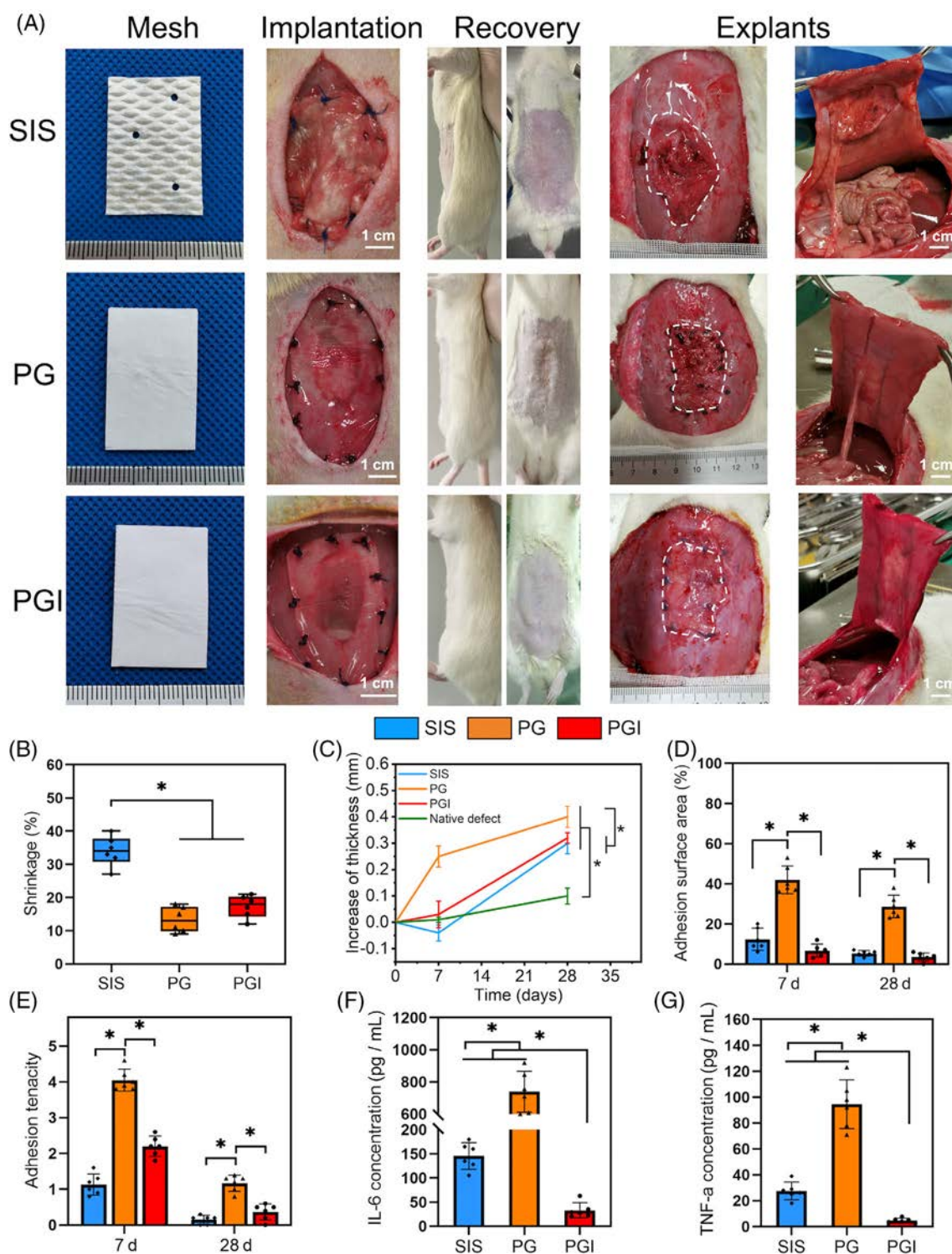
FIGURE 4 Macroscopic observations and inflammatory evaluation. (A) Meshes preparation, implantation, integration, recovery, and retrieval for observation after implantation for 28 days. (B) Shrinkage of the mesh over 28 days. (C) Increase in thickness of mesh over 28 days. (D, E) The evaluation of the adhesion surface area and tenacity over 7 and 28 days. (F, G) The quantification of IL-6 and TNF-α in the exudates at 7 days. White dotted lines indicated the mesh borders. Scale bars represent 1 cm. $n = 6$. *$p < .05$. IBU, Ibuprofen; IL-6, interleukin 6; PGI, PLLA-CL/gelatin/IBU; PLLA-CL, poly(L-lactic acid-co-caprolactone); SIS, small intestinal submucosa; TNF-α, tumor necrosis factor α.

explants at 28 days after implantation ($p < .05$; Figure 4C). After laparotomy, the percentage of adhesion surface areas (%) normalized to the original mesh area was measured, and varying degrees of adhesion tenacity were scored according to the criteria described above. Specifically, the PG explants triggered heavier and broader adhesion than the SIS and PGI explants at 7 and 28 days, respectively ($p < .05$). In
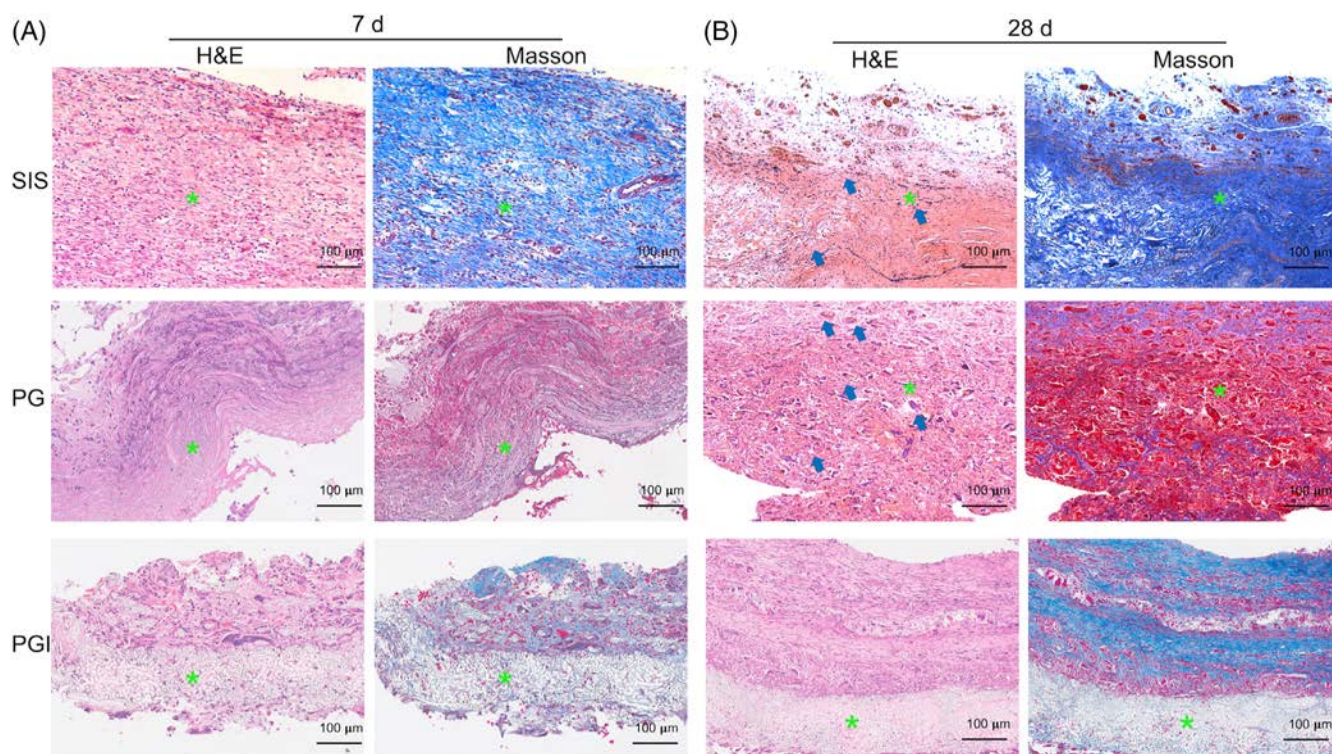
FIGURE 5 Host responses to the explants were analyzed by H&E staining and Masson's trichrome staining. (A) Histological analysis at 7 days after implantation. (B) Histological analysis at 28 days after implantation. Blue arrows indicate foreign body giant cells, and green asterisks indicate the residual implants. IBU, Ibuprofen; H&E, hematoxylin and eosin; PGI, PLLA-CL/gelatin/IBU; PLLA-CL, poly(L-lactic acid-co-caprolactone); SIS, small intestinal submucosa.

contrast, the rats in the PGI group underwent a milder response similar to those in the SIS group during the same period (Figure 4D,E). Furthermore, the concentrations of IL-6 and TNF-α at 7 days, as the initial indicators during the inflammatory response, were lowest in the PGI group ($p < .05$), while the rats in the PG group, without IBU release, triggered the highest level of expression accordingly (Figure 4F,G).

3.5 | Histological analysis

The explants were retrieved for histological analysis to detect the host response and integration at 7 and 28 days after implantation, which were mainly the infiltration of neutrophils, lymphocytes, macrophages, and typical collagen deposition following fibrous capsule formation and ECM remodeling. The representative images of H&E staining revealed that all the meshes triggered the development of granulating tissue at the mesh-tissue interface and induced cell infiltration after 7 days. The observation of the mesh surface facing intraperitoneal cavity further confirmed a more concentrated distribution of predominately mononuclear inflammatory cells deposited over the PG structure than the cells around the PGI mesh. Host cells had been observed to infiltrate into the structure of SIS and PGI to varying extents with collagen deposition. Conversely, fewer collagen filaments were observed to be deposited onto the surface or infiltrated into the

structure of PG with degradation, which was confirmed by Masson's trichrome staining (Figure 5A). After 28 days, all the explants developed to attenuate the inflammatory response. Noticeably, more macrophages fused to form FBGCs, a hallmark of FBR, were detected in the PG mesh compared to the PGI mesh. It implied that the durable FBR presented at the implanted site, with the deposition of sparse and disorganized connective tissue around the mesh (Figure 5B). In contrast, a wavy and lamellar collagen meshwork was identified in the PGI mesh. The images also confirmed that the SIS mesh maintained abundant and well-organized bundles of the collagenous structure after 28 days. The progressive collagenization could be further observed in PGI mesh after 56 days, while the diminishing collagen structure remained in SIS with degradation at the same time (Figure S3).

Within the orchestrated and complicated process of the host response, the expressions of CD11b, CD68, CD86, and CD206 were visualized to reflect the granulocyte and macrophage recruitments and infiltrations (Figure 6A). The immunostaining images of CD11b showed that the PG mesh was heavily infiltrated with mass granulocytes at 7 days after implantation, while the SIS mesh incited granulocyte infiltration more loosely. The quantitative analysis further revealed that both of them triggered more CD11b-positive cell infiltrations than the PGI mesh ($p < .05$; Figure 6B). With the inflammation gradually subsiding, the granulocyte infiltrations in the SIS mesh distributed sparsely and decreased to a level similar to that of the PGI
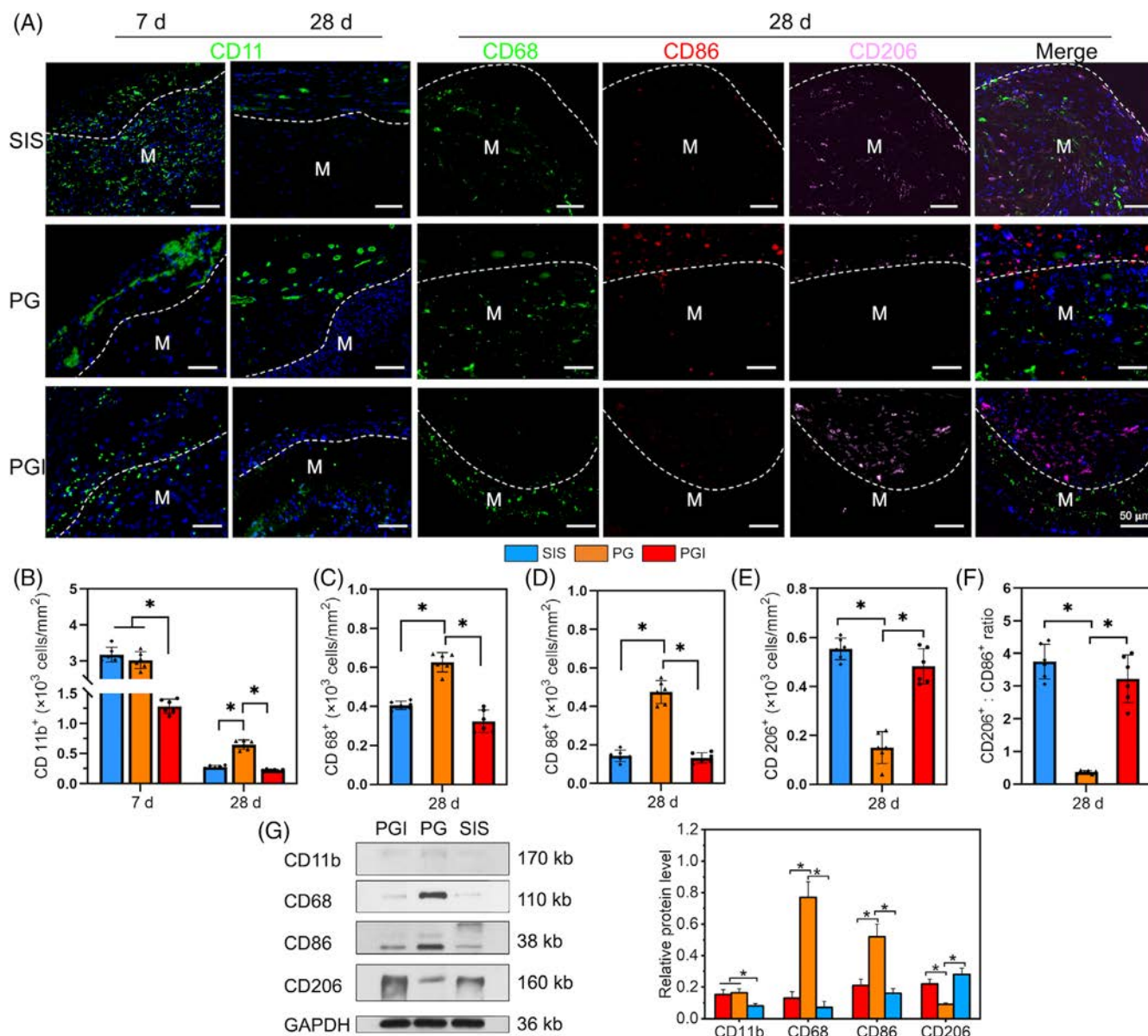
FIGURE 6 Inflammatory responses were detected with immunostaining at 7 and 28 days after implantation. (A) Images of CD11b (green), CD68 (green) CD86 (red), and CD206 (pink) staining of SIS, PG, and PGI explants at 7 and 28 days. (B) Quantification of CD11b-positive cells in the mesh at 28 days. (C) Quantification of CD68-positive cells in the mesh at 28 days. (D) Quantification of CD86-positive cells in the mesh at 28 days. (E) Quantification of CD206-positive cells in the mesh at 28 days. (F) Ratio of CD206:CD86. (G) Quantified analysis of CD11b, CD68, CD86, and CD206 expression by western blotting. M indicated meshes, and the white dotted lines marked the border of mesh with scale bars represent 50 μm in (A). $n = 6$. *$p < .05$. IBU, Ibuprofen; PGI, PLLA-CL/gelatin/IBU; PLLA-CL, poly(L-lactic acid-co-caprolactone); SIS, small intestinal submucosa.

mesh after 28 days. However, the granulocyte infiltration level of PG mesh remained comparatively higher ($p < .05$).

The CD68-positive staining demonstrated the cellular evidence of FBR, such as the macrophages were distributed along with the mesh and infiltrated into it after 28 days. The characteristic expression of CD86 and CD206 was used to identify distinct macrophage subsets, respectively. In specific, the PG mesh induced more prominent recruitments and infiltrations of CD68 positive macrophages with CD86 phenotype than the SIS and PGI meshes after 28 days ($p < .05$; Figure 6C,D), indicating the predominant activation of a pro-inflammatory process within this period. On the contrary, more CD206 phenotype macrophages were visualized in the PGI and SIS meshes than those in the PG mesh ($p < .05$; Figure 6E), guiding the inflammatory response toward the remodeling progression. Furthermore, the ratio of CD206/CD86 that represents the M2/M1 phenotype showed no significant difference between the PGI mesh (3.03 ± 0.89) and the SIS mesh (3.66 ± 0.66), which was higher than that of the PG mesh (0.38 ± 0.05, $p < .05$; Figure 6F). It indicated that the addition of IBU in the PG mesh contributed to attenuating the pro-inflammatory immunoreaction, switching the macrophage polarization
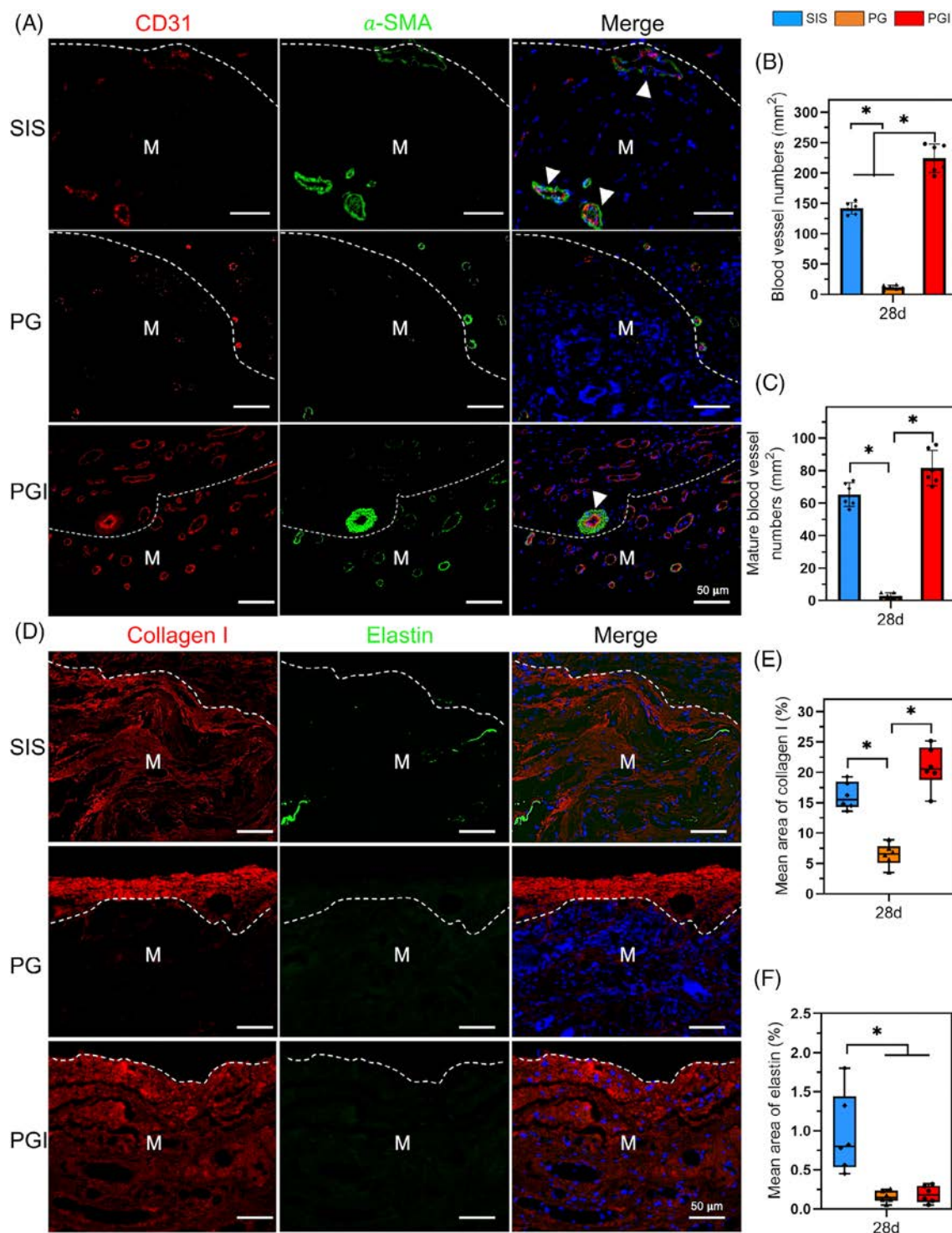
FIGURE 7 Angiogenesis and ECM remodeling of the explants were evaluated by immunostaining at 28 days. (A) CD31 (red) and α-SMA (green) dual immunostaining of the explants at 28 days. (B) Quantification of blood vessel numbers in the mesh at 28 days. (C) Quantification of mature blood vessel numbers in the mesh at 28 days. (D) Collagen I (red) and elastin (green) dual immunostaining of the explants at 28 days. (E) Mean area of collagen I-positive staining in the field at 28 days (%). (F) Mean area of elastin-positive staining in the field at 28 days (%); M indicated meshes, and the white dotted lines marked the border of mesh, white arrows indicated mature blood vessels with scale bars represent 50 μm in (A) and (D). $n = 6$. * $p < .05$. IBU, Ibuprofen; PGI, PLLA-CL/gelatin/IBU; PLLA-CL, poly(L-lactic acid-co-caprolactone); SIS, small intestinal submucosa.

toward a pro-remodeling response. The protein expression analysis was consistent with the immunostaining. The comparison of CD11b, CD68, and CD86 confirmed that the PGI mesh underwent a milder inflammatory response and FBR than the PG mesh. Comparatively, the PGI mesh presented more intensive CD206 expression than the PG mesh ($p < .05$), inducing a more positive pro-remodeling response.

It also indicated that the PGI mesh triggered a host response similar to that of SIS mesh upon those protein expressions ($p > .05$; Figure 6G).

For the angiogenesis evaluation, the permeated blood vessels identified by CD31 immunostaining were measured to calculate the vascular ingrowth in the mesh (Figure 7A). After 28 days of remodeling, the PGI and SIS meshes exhibited notably more intense staining and higher blood vessel numbers than the PG mesh, whereas the PG mesh demonstrated sparse neovascular structures along the mesh at lower density ($p < .05$, Figure 7B). The actin filaments mainly derived from infiltrated myofibroblasts and the phenotype of smooth muscle cells were populated in the tunica media of a mature vessel to maintain its stretchability and flexibility. Therefore, the images of α-SMA staining associated with CD31 staining confirmed that the PGI and SIS groups formed more mature vessel infiltration than the PG group ($p < .05$, Figure 7C). Especially, the vessels in the SIS meshes, composed of capillaries and small veins according to the vessel diameters, obtained higher maturity (0.47 ± 0.03) than those in the PGI meshes (0.37 ± 0.05), which was calculated by the ratio of dual-positive vessels to CD31-positive vessels ($p < .05$).

The expressions of collagen I and elastin with the infiltration of α-SMA positive cells in the structure were visualized to evaluate the ECM remodeling (Figure 7D). The characteristic staining showed that the mature collagen fibers predominating in the PGI and SIS meshes developed a higher percentage of the staining area than those in the PG mesh ($p < .05$; Figure 7E). But the trend was not similar in the analysis of elastin expression. The disorganized elastin fibers with loosely connected were observed in the SIS structure. In contrast, fewer demarcated elastin fibers were detected in the PG and PGI meshes upon quantity ($p < .05$, Figure 7F). It indicated that the addition of IBU in the electrospun PG mesh stabilizes ECM remodeling over the process. Nevertheless, more elastin fibers are assembled in SIS due to its natural ECM and biomolecular cues involved.
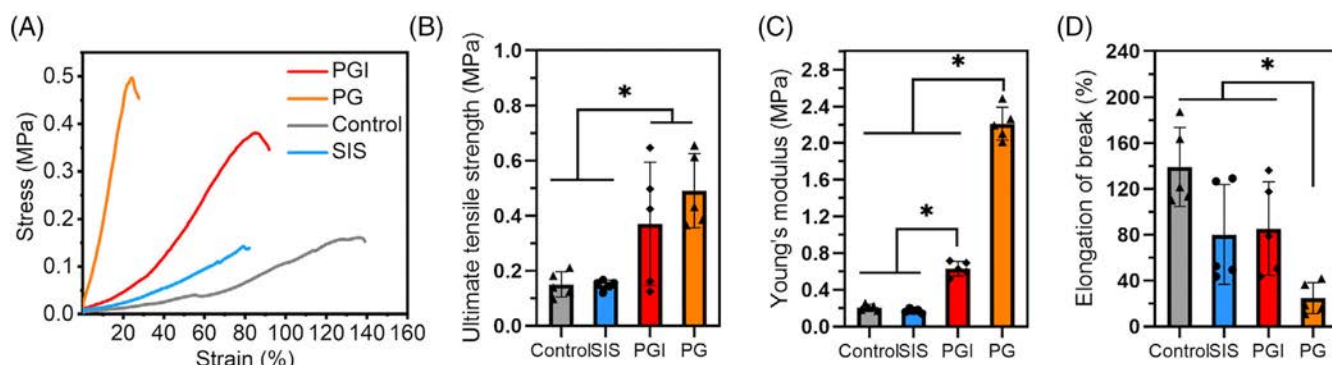
3.6 | Mechanical properties ex vivo

The strain–stress curves indicated that the PG explants exhibited stiffer performances, while the PGI explants were mechanically more compliant through the profound assembly of elastic collagen fibers. However, it has yet been approximated to the counterparts of SIS and the native abdominal wall (control) over 28 days (Figure 8A). The polymeric nanofibers and yarns formed the structure and dominated the passive mechanics of the PGI and PG explants, making their ultimate tensile strength exceed those of the SIS explants and the control ($p < .05$, Figure 8B). Intriguingly, the ultimate tensile strength of PG explants decreased lightly after introducing IBU, which might be attributed to the active tissue integration with passive structure over the remodeling. Conversely, the fibrotic encapsulation surrounding the PG structure with collagen over-deposition might strengthen the mesh. In any event, both electrospun explants displayed adequate strength for the successful defect repair upon the data of the native abdominal wall. The Young's modulus of PG explants was the highest among all, originating from the PG structures that lead to limited incorporation with a stiff encapsulation ($p < .05$, Figure 8C). In contrast, the PGI explants yielded a lower value of Young's modulus and a higher value of elongation of break than the PG explants and resembled the SIS explant and the control more closely after 28 days of remodeling ($p < .05$; Figure 8D).

4 | DISCUSSION

One common challenge hindering the outcome of abdominal wall defect repair is the unfavorable response from the host tissue to the meshes after implantation. Albeit, the prestigious meshes have been used overwhelmingly for hernia treatment, the triggering of host response to facilitate retrieving physiological functions remain a conundrum. Even the fatal removal of the undegraded mesh and complete debridement of the surrounding tissues could result in a long trauma recovery process.[27] Therefore, mesh preparation and functionalization to regulate host response are always a primary concern.[28] Along with the rapid development of biological scaffold over decades, the decellularized SIS mesh is reportedly preponderant in the host response owing to its ECM structure coupled with bioactive molecules, which is much more intriguing than the polymeric mesh for modulating pro-remodeling macrophages.[29] Especially, the intraperitoneal adhesion could be alleviated under a mild pro-inflammatory response. However, SIS is controversial for supporting constructive remodeling to eventually avoid bulges, herniation, or recurrence, and the heterogeneity of ECM resources, immunogenicity, surgical handling, and costs.[5] In contrast, the electrospun mesh composed of degradable fibers tailored with a biocompatible surface could provide tissue-matched mechanical strength conferred to the ECM-like structure in a subtle strategy.[30] In our early works, we have functionalized the electrospun meshes with biomechanics-matched,[31] integration-enhanced,[32] antibacterial,[33] and antiadhesive features[34] to improve abdominal wall defect repair, respectively. These highlight the versatile processibility of electrospinning and thereby prompt us to reckon with host response by fabricating a functional electrospun mesh via introducing FBR-attenuated substances. Herein, we address this topic of host response modulation for intraperitoneal repair in the comparison of a commercial SIS with a tailored functional mesh.

By investigating mechanically sufficient and cell-friendly polymers, PLLA-CL and gelatin have been selected to fabricate the electrospun mesh through a practicable procedure.[35] Herein, PLLA-CL was mixed with gelatin proportionally to improve the mechanical properties, biocompatibility, and controllable degradability of the structure as a desirable template for loading IBU. In this context, the postoperative administration of IBU is expected to reduce the inflammation triggered by the implants and limit the collagen over-deposition by modulating the macrophage-driven FBR.[36,37] The PGI mesh is tailored with a bilayer structure, in which a large surface area of nanofiber layer ensures the loading efficiency and the continuous release of IBU in a stable system. Furthermore, the smooth and biocompatible surface of this layer potentially reduces the risk of tissue

FIGURE 8   Representative mechanical properties of the explants after 28 days. (A) Stress–strain curves; (B) Ultimate tensile strength; (C) Young's modulus; and (D) Elongation of break. $n = 5$. *$p < .05$. IBU, Ibuprofen; PGI, PLLA-CL/gelatin/IBU; PLLA-CL, poly(L-lactic acid-co-caprolactone); SIS, small intestinal submucosa.

adhesion, while the porous yarn layer could promote cell infiltration and tissue integration effectively.

After implantation, macroscopic observation of the PGI mesh presented parietal peritoneal recovery, while the presence of PG mesh showed an encapsulated healing with a greater increase in thickness. This finding is attributed to the ineffective incorporation under an aggressive and persistent response to the PG mesh, leading to a heavier intraperitoneal adhesion. In the inflammatory phase of host response, the expression of pro-inflammatory cytokines escalates cell differentiation and the imbalance between tissue plasminogen activators and plasminogen activator inhibitors.[38] In this context, it develops the collagen and fibroin accumulation on the mesh surface and visceral peritoneum thereby resulting in intraperitoneal adhesion between them. In contrast, the release of IBU from the PGI mesh attenuated the infiltration of granulocytes characterized by CD11b$^+$ staining prominently.

Within the highly orchestrated inflammatory activation, the adsorption of serum proteins to the mesh surface creates a chemoattractant gradient for neutrophils and monocytes, and macrophages.[39] Under this inflammatory environment, the pro-inflammatory macrophage phenotype can be triggered through TNF-α and IL-6 and other cytokines, and the over-activation or sustained mobilization of them undoubtedly impairs tissue healing.[40] In this study, the administration of IBU in the PGI mesh diminished the initial expression of TNF-α and IL-6 substantially, maintaining the level of inflammatory reaction characterized by granulocytes and macrophages milder than that of the PG mesh. Intriguingly, the SIS mesh as a biological paradigm also incited heavy CD11 positive cell infiltration with the high initial expression of TNF-α and IL-6, although there was no significant difference between SIS and PGI mesh. The initial response after SIS implantation is attributed to the fact that SIS remains a xenograft that induces an immune response at the biomaterial-tissue interface, and the active biomolecules in SIS-ECM could incite this response to some extent.[41] In fact, the inflammatory response is also essential for the repair process, making it an attractive target to leverage for biomaterial–tissue integration. Of note, several studies have shown that the SIS-ECM is infiltrated with a greater proportion of M2 macrophage

than the polymeric meshes, which is also verified in this study by the comparison of CD206/CD86 between the SIS and PG meshes. It is considered that the recruitment of endogenous stem cells, growth factor sequestration, and release of bioactive fragments with degradation all contribute to modulating macrophage polarization in the innate immune response.[22] Recently, the ECM-derived extracellular vesicles, namely matrix-bound nanovesicles, have been proven to recapitulate the effects of whole ECM associated with the functional capacities of modulating anti-inflammatory, pro-remodeling M2 macrophages.[42] However, the underlying mechanisms are not fully understood, making it still challenging to tease out an optimal strategy for FBR reduction by integrating critical determiners with off-the-shelf mesh, especially regarding clinical translation, surgical handling, and medical cost. Whereas the PGI mesh prepared in this study offers feasible modifications and solutions for these problems.

In accordance with the inflammatory and FBR evaluation, the PGI mesh developed a more favorable remodeling than the PG mesh owing to the M2 macrophage-superior response over this period. The vascularized and collagenized progress was observed at the center of the PGI structures, indicating an advanced remodeling. In contrast, most of the events that occurred surrounding the PG mesh represented the tendency of encapsulation. The M2 macrophage-dominated response helps SIS to assemble collagen fibrils similar to the PGI mesh. However, SIS also benefits from its original ECM structure without full degradation, making the underlying mechanisms of remodeling different from the electrospun mesh. Based on IBU administration, the functional electrospun template aims to relieve the initial inflammatory response followed by a pro-remodeling response, while the biological template facilitates a pro-remodeling response based on its ECM structure with diminishing inflammation. After the degradation of ECM, the remodeling of SIS might not further afford its structure loss. The mechanical measurements validated that the SIS mesh yielded insufficient strength to exceed that of the native abdominal wall. Comparatively, the mechanical strength afforded by the PGI mesh was superior to the SIS mesh, with comparable elongation obtained through the progressive incorporation of smooth muscle cells, collagen, and elastin into the structure.

Although this study presents outstanding behaviors of a functional mesh for abdominal wall defect repair, several potential limitations should be addressed in further studies. Specifically, M1 and M2 macrophages were simply identified by single surface markers, whereas, M2 macrophages can be subdivided into M2a, M2b, and M2c subtypes featuring distinct immunoregulatory functions through polarization.[43] CD206 positive macrophage generally represents the M2a phenotype and is involved in ECM remolding by expressing relevant cytokines to promote wound healing, while M2b and M2c could help to suppress scarring formation through the secretion of IL-10.[44] For a better understanding of immunomodulatory, the markers of other M2 subtypes and their potential roles in the process, including the activation of macrophages with controlled timing and the modulation of their interactions with other cell types involved, should be documented as a dynamic other than a static process by more comprehensive and in-depth studies. Regarding the known understanding of anti-inflammatory and immunoregulation of IBU, it exerts anti-inflammatory effects through inhibition of prostaglandin E2 (PGE2) production. These processes inhibit the M1 macrophage polarization through suppression of PGE2 and downstream activation of the IL-6/PMN/ Th-17 cascade.[45] In the IBU-aided strategy, the timely inhibition of pro-inflammatory cytokines provides a milieu for facilitating pro-remodeling responses. However, the mechanism of shifting macrophage phenotype upon IBU is still unclear. In addition, the anti-infective and mechanical properties of a slow-degraded mesh need to be evaluated over a long-term study, with mesh applicability being investigated in large animals.

5 | CONCLUSIONS

In this study, we successfully fabricated a functional mesh by integrating IBU with PG capable of modulating host response during tissue remodeling, further demonstrating its potential applications for full-thickness abdominal wall defect repair in a rat model. The proportional combination of PLLA-CL and gelatin, as the template of the functional mesh, is characterized to regulate its bilayer structure with the mechanical properties adequate for in vivo repair. The sustained release of IBU from the template over 21 days in vitro potentially conferred inflammation-alleviating function to the mesh. The host response and integration in vivo demonstrated that the PGI mesh showed a better performance than the PG mesh by attenuating the inflammatory response, FBR, and relieving intraperitoneal adhesion while accelerating angiogenesis and ECM remodeling over 28 days after implantation. The PGI mesh initiated a pro-remodeling response similar to the SIS mesh, while providing preponderant mechanical supports over the SIS mesh and native abdominal wall. Collectively, the functional mesh fabricated in this study reckons with the problem of the host response to the conventional polymers and sheds light on the advanced functionalization for mesh repair.

AUTHOR CONTRIBUTIONS

Jiajie Liu, Rui Tang, and Qiaolin Ma: Methodology; data curation; statistical analysis; writing—original draft preparation. Jinglei Wu: Visualization and investigation. Zhengni Liu: Supervision; conceptualization; writing—reviewing and editing. Xiaoqiang Zhu: Software. Jiajie Liu and Rui Tang contributed equally to this work. The manuscript was written through the contributions of all authors. All authors have approved the final version of the manuscript.

ACKNOWLEDGMENTS

CONFLICT OF INTEREST STATEMENT

The authors declare no conflicts of interest.

DATA AVAILABILITY STATEMENT

The data that support the findings of this study are available from the corresponding author upon reasonable request.

ORCID

Jinglei Wu 🄓 https://orcid.org/0000-0001-9549-3992

REFERENCES

1. HerniaSurge Group. International guidelines for groin hernia management. *Hernia*. 2018;22:1-165.
2. Pawlak M, Bury K, Śmietański M. The management of abdominal wall hernias—in search of consensus. *Wideochir Inne Tech Maloinwazyjne*. 2015;10:49-56.
3. Liu Z, Wei N, Tang R. Functionalized strategies and mechanisms of the emerging mesh for abdominal wall repair and regeneration. *ACS Biomater Sci Eng*. 2021;7:2064-2082.
4. Mulier KE, Nguyen AH, Delaney JP, Marquez S. Comparison of Permacol™ and Strattice™ for the repair of abdominal wall defects. *Hernia*. 2011;15:315-319.
5. Ho CH, Liao PW, Yang SS, et al. The use of porcine small intestine submucosa implants might be associated with a high recurrence rate following laparoscopic herniorrhaphy. *J Formos Med Assoc*. 2015;114:216-220.
6. Klosterhalfen B, Klinge U, Schumpelick V. Functional and morphological evaluation of different polypropylene-mesh modifications for abdominal wall repair. *Biomaterials*. 1998;19:2235-2246.
7. Nolfi AL, Brown BN, Liang R, et al. Host response to synthetic mesh in women with mesh complications. *Am J Obstet Gynecol*. 2016;215: 206-206.e8.
8. Nolfi AL, Brown BN, Liang R, et al. Host response to synthetic mesh in women with mesh complications. *Am J Obstet Gynecol*. 2016; 215(206):e1-e8.
9. Pineda Molina C, Giglio R, Gandhi RM, et al. Comparison of the host macrophage response to synthetic and biologic surgical meshes used for ventral hernia repair. *J Immunol Regener Med*. 2019;3:13-25.
10. Marinaro F, Sánchez-Margallo FM, Álvarez V, et al. Meshes in a mess: mesenchymal stem cell-based therapies for soft tissue reinforcement. *Acta Biomater*. 2019;85:60-74.
11. Brown BN, Londono R, Tottey S, et al. Macrophage phenotype as a predictor of constructive remodeling following the implantation of biologically derived surgical mesh materials. *Acta Biomater*. 2012;8: 978-987.
12. Blázquez R, Sánchez-Margallo FM, Álvarez V, Usón A, Casado JG. Surgical meshes coated with mesenchymal stem cells provide an anti-inflammatory environment by a M2 macrophage polarization. *Acta Biomater*. 2016;31:221-230.

13. Blázquez R, Sánchez-Margallo FM, Álvarez V, Usón A, Marinaro F, Casado JG. Fibrin glue mesh fixation combined with mesenchymal stem cells or exosomes modulates the inflammatory reaction in a murine model of incisional hernia. *Acta Biomater*. 2018;71:318-329.

14. Belyansky I, Tsirline VB, Montero PN, et al. Lysostaphin-coated mesh prevents staphylococcal infection and significantly improves survival in a contaminated surgical field. *Am Surg*. 2011;77:1025-1031.

15. Sanbhal N, Li Y, Khatri A, Peerzada M, Wang L. Chitosan cross-linked bio-based antimicrobial polypropylene meshes for hernia repair loaded with levofloxacin HCl via cold oxygen plasma. *Coatings*. 2019;9:168.

16. Manrique-Moreno M, Heinbockel L, Suwalsky M, Garidel P, Brandenburg K. Biophysical study of the non-steroidal anti-inflammatory drugs (NSAID) ibuprofen, naproxen and diclofenac with phosphatidylserine bilayer membranes. *Biochim Biophys Acta*. 2016;1858:2123-2131.

17. Lima AF, Pegorin GS, Miranda MCR, et al. Ibuprofen-loaded biocompatible latex membrane for drug release: characterization and molecular modeling. *J Appl Biomater Funct Mater*. 2021;19:22808000211005383.

18. Yuan Z, Zhao J, Zhu W, et al. Ibuprofen-loaded electrospun fibrous scaffold doped with sodium bicarbonate for responsively inhibiting inflammation and promoting muscle wound healing in vivo. *Biomater Sci*. 2014;2:502-511.

19. Pires LR, Guarino V, Oliveira MJ, et al. Ibuprofen-loaded poly(trimethylene carbonate-co-ε-caprolactone) electrospun fibres for nerve regeneration. *J Tissue Eng Regen Med*. 2016;10:E154-E166.

20. Mao Y, Chen M, Guidoin R, et al. Potential of a facile sandwiched electrospun scaffold loaded with ibuprofen as an anti-adhesion barrier. *Mater Sci Eng C Mater Biol Appl*. 2021;118:111451.

21. FitzGerald JF, Kumar AS. Biologic versus synthetic mesh reinforcement: what are the pros and cons? *Clin Colon Rectal Surg*. 2014;27:140-148.

22. Rowley AT, Nagalla RR, Wang SW, Liu WF. Extracellular matrix-based strategies for immunomodulatory biomaterials engineering. *Adv Healthc Mater*. 2019;8:e1801578.

23. Wang Y, Zheng G, Xie X, et al. Low-dose celecoxib-loaded PCL fibers reverse intervertebral disc degeneration by up-regulating CHSY3 expression. *J Nanobiotechnology*. 2023;21:76.

24. Li H, Wang X, Liu J, et al. Nanofiber configuration affects biological performance of decellularized meniscus extracellular matrix incorporated electrospun scaffolds. *Biomed Mater*. 2021;16:65013.

25. Jenkins SD, Klamer TW, Parteka JJ, Condon RE. A comparison of prosthetic materials used to repair abdominal wall defects. *Surgery*. 1983;94:392-398.

26. Deeken CR, Lake SP. Mechanical properties of the abdominal wall and biomaterials utilized for hernia repair. *J Mech Behav Biomed Mater*. 2017;74:411-427.

27. Klosterhalfen B, Klinge U. Retrieval study at 623 human mesh explants made of polypropylene—impact of mesh class and indication for mesh removal on tissue reaction. *J Biomed Mater Res B Appl Biomater*. 2013;101:1393-1399.

28. Boire R. Predictive analytics: the power to predict who will click, buy, lie, or die. *J Market Anal*. 2013;1:184-185.

29. Fujii M, Tanaka R. Porcine small intestinal submucosa alters the biochemical properties of wound healing: a narrative review. *Biomedicine*. 2022;10:2213.

30. Glindtvad C, Chen M, Vinge Nygaard J, et al. Electrospun biodegradable microfibers induce new collagen formation in a rat abdominal wall defect model: a possible treatment for pelvic floor repair? *J Biomed Mater Res B Appl Biomater*. 2018;106:680-688.

31. Liu Z, Liu J, Liu N, Zhu X, Tang R. Tailoring electrospun mesh for a compliant remodeling in the repair of full-thickness abdominal wall defect—the role of decellularized human amniotic membrane and silk fibroin. *Mater Sci Eng C Mater Biol Appl*. 2021;127:112235.

32. Liu Z, Liu X, Bao L, et al. The evaluation of functional small intestinal submucosa for abdominal wall defect repair in a rat model: potent effect of sequential release of VEGF and TGF-β1 on host integration. *Biomaterials*. 2021;276:120999.

33. Liu Z, Zhu X, Tang R. Electrospun scaffold with sustained antibacterial and tissue-matched mechanical properties for potential application as functional mesh. *Int J Nanomedicine*. 2020;15:4991-5004.

34. Liu Z, Zhu X, Zhu T, Tang R. Evaluation of a biocomposite mesh modified with decellularized human amniotic membrane for intraperitoneal onlay mesh repair. *ACS Omega*. 2020;5:3550-3562.

35. Sun Y, Li X, Liu S, et al. Fabrication and properties of PLLA-gelatin nanofibers by electrospinning. *J Appl Polym Sci*. 2010;117:542-547.

36. Meek IL, Van de Laar MA, Vonkeman HE. Non-steroidal anti-inflammatory drugs: an overview of cardiovascular risks. *Pharmaceuticals (Basel)*. 2010;3:2146-2162.

37. Lee JH, Go AK, Oh SH, Lee KE, Yuk SH. Tissue anti-adhesion potential of ibuprofen-loaded PLLA-PEG diblock copolymer films. *Biomaterials*. 2005;26:671-678.

38. Heissig B, Salama Y, Takahashi S, Osada T, Hattori K. The multifaceted role of plasminogen in inflammation. *Cell Signal*. 2020;75:109761.

39. Ogle ME, Segar CE, Sridhar S, Botchwey EA. Monocytes and macrophages in tissue repair: implications for immunoregenerative biomaterial design. *Exp Biol Med (Maywood)*. 2016;241:1084-1097.

40. Ye J, Xie C, Wang C, et al. Promoting musculoskeletal system soft tissue regeneration by biomaterial-mediated modulation of macrophage polarization. *Bioact Mater*. 2021;6:4096-4109.

41. Allman AJ, McPherson TB, Badylak SF, et al. Xenogeneic extracellular matrix grafts elicit a TH2-restricted immune response. *Transplantation*. 2001;71:1631-1640.

42. Crum RJ, Hall K, Molina CP, et al. Immunomodulatory matrix-bound nanovesicles mitigate acute and chronic pristane-induced rheumatoid arthritis. *NPJ Regen Med*. 2022;7:13.

43. Dervan A, Franchi A, Almeida-Gonzalez FR, et al. Biomaterial and therapeutic approaches for the manipulation of macrophage phenotype in peripheral and central nerve repair. *Pharmaceutics*. 2021;13:2161.

44. Wei F, Liu S, Chen M, et al. Host response to biomaterials for cartilage tissue engineering: key to remodeling. *Front Bioeng Biotechnol*. 2021;9:664592.

45. Pennock ND, Martinson HA, Guo Q, et al. Ibuprofen supports macrophage differentiation, T cell recruitment, and tumor suppression in a model of postpartum breast cancer. *J Immunother Cancer*. 2018;6:98.

SUPPORTING INFORMATION

Additional supporting information can be found online in the Supporting Information section at the end of this article.